ORIGINAL ARTICLE

High Efficiency Onboard Charger Based on Two-Stage Circuit

Fei Xue[1] · Xin Ma[1] · Hongqiang Li[1] · Di Zhang[1] · Hengshan Xu[2] · Lei Zhou[1] · Chao Wang[1]

Abstract

On-board charger (OBC) is key part of electric vehicles. Limited to space and weight, design objectives of OBC are high power-density and high efficiency. Two-stage circuit is commonly used for 3.3 kW OBC, interleaved power factor correction (ILPFC) is utilized for power factor correction and DC bus voltage regulation, LLC resonant converter is utilized for voltage and power regulations. In this paper, the relationships between the internal parameters and efficiency of ILPFC are studied by discrete iterative method, and the internal parameters are optimized to improve ILPFC`s efficiency. Meanwhile, the relationships between the resonant parameters and efficiency of LLC converter are also studied by fundamental harmonic approximation method to optimize the efficiency in wide charging voltage. A 3.3 kW OBC prototype is developed to verify the effectiveness and correctness of the optimal method, the power factor and total harmonic distortion at full-load state are about 99.99% and 2.98% with the charging voltage ranging from 230 to 430 V, respectively.

Keywords On-board charger · Power density · Efficiency · Electric vehicles

1 Introduction

Limited to space and weight, main design objectives of OBC are high power density [1–6], high efficiency [7–9], high power factor (PF) [10], and low total harmonic distortion (THD) [11–13]. Typical OBC is based two-stage circuit [14–16], AC/DC stage is used for power factor correction [17], DC/DC stage is utilized to regulate charging power and voltage [18]. Traditional single phase boost circuit has high current stress [19], and large inductor [20]. On contrary, interleaved boost power factor correction (ILPFC) has little current ripple, small inductor [21], high efficiency, and high power-density [20]. LLC converter has merits of soft-switching [22], high efficiency [23, 24], and wide voltage [25], then ILPFC + LLC converter is suitable for OBC [26]. However, the efficiency is affected by switching frequency, boost inductors, and DC link voltage [27], which determines conduction loss and switching loss, and the above losses are difficult to analyze by traditional method.

To improve OBC`s efficiency, there are commonly three methods: (a) high performance devices [14, 18, 28–30], (b) modified circuit [6, 22, 31–33], and (c) improved control [1, 34, 35]. High performance devices is the most direct approach, literatures [14, 28, 29] use SiC and GaN devices to improve the efficiency, however, presently, the cost of these devices is much higher than Si-based devices, which is the biggest obstacle for industrial application. To improve the efficiency, literature [10] proposed variable dc-link voltage control and ensure LLC converter at the resonant frequency in wide voltage range, however, which brings complex control to PFC. Literature [26] designed an OBC with considering efficiency and volume, however, the peak efficiency of LLC converter is 95.4% and needs further improvement. Hybrid control adopted in [1] and [2] can improve the peak efficiency of LLC converter to 96%, but the control is complex and not good for applications. Ultrawide dc-link voltage in [36] is also useful for efficiency, but the volume of passive components maybe increased because the large current at low charging voltage. Multi-resonant frequency is introduced in [37] to widen the charging voltage range, but the extra components results in the complex hardware, low reliability, and difficulty to design the multi-parameters. The above methods are useful to improve the efficiency, but it is hard to deal with the contradictions between hardware`s

✉ Hengshan Xu
  810228706@qq.com

[1] Electric Power Research Institute of State Grid Ningxia Electric Power Co., Ltd, Yinchuan, China

[2] College of Electrical Engineering & New Energy, China Three Gorges University, Yichang, China

cost, complexity, reliability, control, implementation, and so on.

To improve the efficiency in wide charging voltage range without increasing hardware cost and control complexity, a discrete iterative method is proposed to estimate and optimize ILPFC`s efficiency. Moreover, LLC converter`s loss and efficiency in wide charging voltage range are also estimated and optimized based on fundamental harmonic approximation (FHA). The OBC`s efficiency in wide charging voltage range is optimized by designing the internal parameters of ILPFC and LLC converters.

2 ILPFC

Typical topology for OBC includes two stages, as Fig. 1 shows. AC/DC is used for PFC, DC/DC is used for output voltage and power regulation. Actually, the topology in Fig. 2 is commonly adopted. V_{AC}, i_{AC} and V_{BUS} are input voltage, input current and DC link voltage. L_1, L_2 are boost inductors, $L_1 = L_2 = L_b$. $D_1 \sim D_4$ are rectifier diodes. $Q_1 \sim Q_2$ and $D_5 \sim D_6$ are MOSFETs and freewheeling diodes. $S_1 \sim S_2$ are control signals of $Q_1 \sim Q_2$, they have a phase difference of 180 degree. $i_{L1} \sim i_{L2}$ and $i_{Q} \sim i_{Q2}$ are the currents of boost inductor and MOSFET. $i_{s,PFC}$ is bridge current and $i_{s,PFC} = i_{L1} + i_{L2}$. C_B is link capacitor. $Q_3 \sim Q_6$ and $D_7 \sim D_{10}$ are LLC converter`s MOSFETs and diodes. L_m, L_r and C_r are magnetizing inductor, resonant inductor and capacitor. v_{ab}
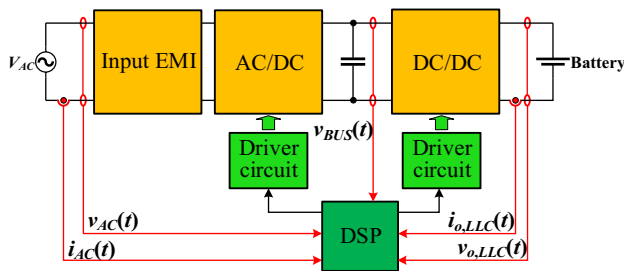
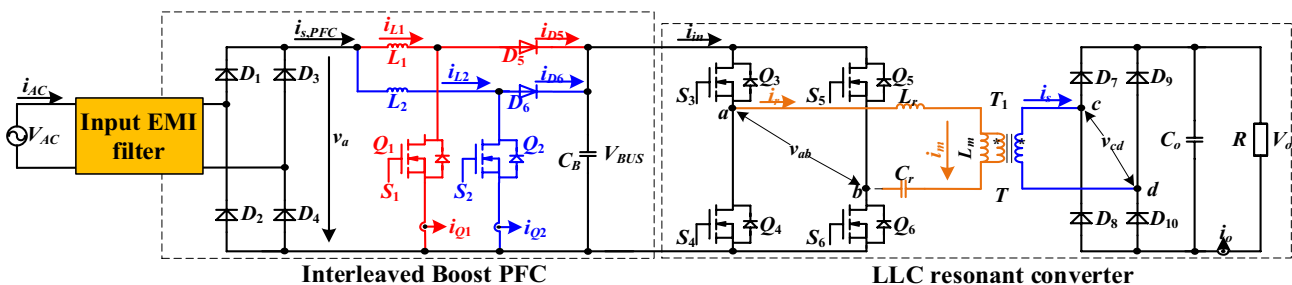and v_{cd} are primary and secondary-side ac voltages. i_r and i_o are resonant and output currents. V_o is charging voltage, C_o is output capacitor.

Losses of EMI filters, rectifier bridge, boost inductors, MOSFETs and diodes of ILPFC are denoted as $P_{E, loss}$, $P_{b, loss}$, $P_{Lb, loss}$, $P_{d, PFC, loss}$ and $P_{m, PFC, loss}$. $f_{s, PFC}$ is switching frequency, the sampling period is $t_{s, PFC} = 1/f_{s, PFC}$. v_a is discrete as Σv_k, k is sampling series, the sampling time is Σt_k. In a sampling period, $v_a(t)$ can be seen as constant value. $i_{L1}(t)$, v_a and S_1 are shown in Fig. 3 [17–19].

2.1 Current Waveforms of IBPFC

2.1.1 Current Waveforms in CCM

In a half line period, as Fig. 3a shows, $i_{L1}(t)$ is continuous and the average is $0.5i_{AC}(t)$. In the kth switching period, $i_{L1}(t)$ linearly increases when $d_{k-1} = 1$ and decreases when $d_{k-1} = 0$. $I_{k, start}$ and $I_{k, end}$ are the starting and ending values of $i_{L1}(t)$. $i_{L1, kr}$ and $i_{L1, kf}$ are waveforms when $d_{k-1} = 1$ and $d_{k-1} = 0$. t_{k-1} and t_k are the starting time and ending time. $I_{k,}$turnoff is turn-off current of Q_1, $T_{k, r}$ and $T_{k, f}$ are the turn-on and turn-off time. $i_{m1, k}(t)$, $i_{d5, k}(t)$ and $i_{L1, k}(t)$ are currents of Q_1, D_5 and L_1. Duty cycle of Q_1 is [20]

$$d_k = (V_{BUS} - v_k)/V_{BUS} \qquad (1)$$

During $t_{k-1} \leq t \leq t_{k-1} + d_k t_{s, PFC}$, $i_{L1,k}(t)$ raises in the slope of v_k/L. $i_{m1,k}(t) = i_{L1,k}(t)$, and $i_{d5,k}(t) = 0$. During $t_{k-1} + d_k t_{s,PFC} \leq t \leq t_k$, $i_{L1,k}(t)$ decreases in the slope of $(V_{BUS} - v_k)/L$. $i_{m1,k}(t) = 0$. $i_{d5,k}(t) = i_{L1,k}(t)$. Because $I_{k,start} = I_{k-1,end}$, then $i_{L1}(t)$, $i_{m1}(t)$ and $i_{d5}(t)$ in the kth switching period in CCM can be expressed as (2), where $T_{k,f} = (1 - d_k)t_{s,PFC}$. $T_{k,r} = d_k t_{s,PFC}$. Because $I_{k+1, start} = I_{k,end}$, then $i_{L1}(t)$, $i_{m1}(t)$ and $i_{d5}(t)$ can be expressed as (3), where f_{line} is the line frequency. By the same principle, $i_{m2}(t)$, $i_{d6}(t)$ and $i_{L2}(t)$ in CCM can be also obtained.
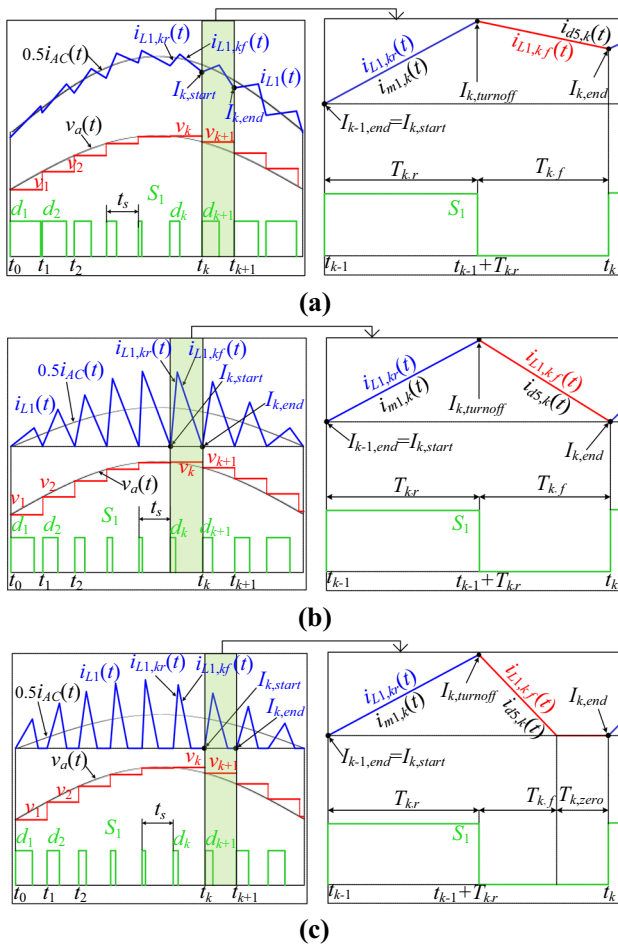

Fig. 1 Diagram of on-board charger

Fig. 2 Topology of OBC with two-stage circuit

Fig. 3 Waveforms of $i_L(t)$, $v_a(t)$ and S_1 in: **a** CCM, **b** BCM, and **c** DCM in half line period

2.1.2 Currents Waveforms in BCM

As Fig. 3b shows, in BCM, at the starting and ending points, $i_{L1}(t) = 0$, the duty cycle is $d_k = (V_{BUS} - v_k)/V_{BUS}$. At $t = t_{k-1}$ and $t = t_k$, $i_{L1}(t) = 0$, and $I_{k,start} = I_{k,end} = I_{k-1,end} = I_{k+1,start} = 0$. During $t_{k-1} \leq t \leq t_{k-1} + d_k t_{s,PFC}$, $i_{L1,k}(t)$ raises in the slope of v_k/L, $i_{m1,k}(t) = i_{L1,k}(t)$, $i_{d5}(t) = 0$. During $t_{k-1} + d_k t_{s,PFC} < t < t_k$, $i_{L,k}(t)$ decreases in the slope of $(V_{BUS} - v_k)/L$. $i_{m1,k}(t) = i_{L1,k}(t)$. $i_{d5,k}(t) = 0$. $i_{m1}(t)$, $i_{d5}(t)$ and $i_{L1}(t)$ in the kth period are

$$
\begin{cases}
I_{k,start} = 0 & t = t_{k-1} \\
i_{m1,k}(t) = I_{k,start} + v_k[t - (k-1)t_{s,PFC}]/L_b & t_{k-1} < t \leq t_{k-1} + d_k t_{s,PFC} \\
i_{m1,k}(t) = 0 & t_{k-1} + d_k t_{s,PFC} < t \leq t_k \\
i_{d5,k}(t) = 0 & t_{k-1} < t \leq t_{k-1} + d_k t_{s,PFC} \\
\quad i_{d5,k}(t) = I_{k,start} + v_k T_{k,r}/L_b & \\
\quad -(V_{BUS} - v_k)[t - (k-1)t_{s,PFC} - T_{k,r}]/L_b & t_{k-1} + d_k t_{s,PFC} < t \leq t_k \\
I_{k,turnoff} = I_{k,start} + T_{k,r}/L_b & t = t_{k-1} + d_k t_s \\
I_{k,end} = I_{k+1,start} = 0 & t = t_k
\end{cases}
\tag{4}
$$

2.1.3 Currents Waveforms in DCM

As Fig. 3c shows, in the kth switching period, $i_{L1,k}(t)$ is 0 before the end, during $t_{k-1} \leq t < t_{k-1} + d_k t_{s,PFC}$, $i_{L1,k}(t)$ increase in the slope of v_k/L. $i_{m1,k}(t) = i_{L1,k}(t)$. $i_{d5}(t) = 0$. Q_1 is turned off at $t = t_{k-1} + d_k t_{s,PFC}$. During $t_{k-1} + d_k t_{s,PFC} \leq t < t_{k,PFC} + T_{k,r} + T_{k,f}$, $i_{L1,k}(t)$ decreases in the slope of $(V_{BUS} - v_k)/L$. $i_{d5}(t) = i_{L1,k}(t) = 0$ at $t = t_{k-1} + T_{k,r} + T_{k,f}$. During $t_{k-1} + T_{k,r} + T_{k,f} \leq t < t_k$, $i_{L1,k}(t)$ is in DCM, $i_{L1,k}(t) = i_{d5,k}(t) = i_{m1,k}(t) = 0$. And d_k in DCM and the average current $I_{L1\_k\_av}$ are give by (5) and (6) [21], where $P_{o,PFC}$ is output power. $i_{m1}(t)$, $i_{d5}(t)$ and $i_{L1}(t)$ in kth switching period in DCM are expressed as (7). Once $i_{m1}(t)$, $i_{d5}(t)$ and $i_{L1}(t)$ are obtained, RMS values of $i_{m1}(t)$, $i_{d5}(t)$ and $i_{L1}(t)$ can be calculated by (8), where I_{L1}, I_{d5}, I_{m1} and $I_{s,PFC}$ are RMS currents of L_1, D_5

$$
\begin{cases}
I_{k,start} = I_{k-1,end} & t = t_k \\
i_{m1,k}(t) = I_{k,start} + v_k[t - (k-1)t_{s,PFC}]/L_b & t_{k-1} < t \leq t_{k-1} + d_k t_{s,PFC} \\
i_{m1,k}(t) = 0 & t_{k-1} + d_k t_{s,PFC} < t \leq t_k \\
i_{d5,k}(t) = 0 & t_{k-1} < t \leq t_{k-1} + d_k t_{s,PFC} \\
\quad i_{d5,k}(t) = I_{k,start} + v_k T_{k,r}/L_b & \\
\quad -(V_{BUS} - v_k)[t - (k-1)t_{s,PFC} - T_{k,r}]/L_b & t_{k-1} + d_k t_{s,PFC} < t \leq t_k \\
I_{k,turnoff} = I_{k,start} + T_{k,r}/L_b & t = t_{k-1} + d_k t_{s,PFC} \\
I_{k,end} = I_{k,start} + [v_k T_{k,r} + (V_{BUS} - v_k)T_{k,f}]/L_b & t = t_k
\end{cases}
\tag{2}
$$

$$
\begin{cases}
i_{m1}(t) = \sum_{k=1}^{2f_s/f_{line}} \{i_{m1,k}(t)\} \\
i_{d5}(t) = \sum_{k=1}^{2f_s/f_{line}} \{i_{d5,k}(t)\} \\
i_{L1}(t) = i_{m1}(t) + i_{d5}(t)
\end{cases}
\tag{3}
$$

and M_1, respectively.

$$
d_k = \frac{2\sqrt{L_b f_{s,PFC} P_{o,PFC}}}{\sqrt{2} V_{AC}} \sqrt{1 - \frac{v_k}{V_{BUS}}}
\tag{5}
$$

$$
I_{L1\_k\_av} = \sqrt{2} P_{o,PFC} \sin(2\pi f_{line} t_{s,PFC} k)/(2 V_{AC})
\tag{6}
$$

$$\begin{cases} I_{k,start} = 0 & t = t_{k-1} \\ i_{m1,k} = I_{k,start} + v_k[t - (k-1)t_{s,PFC}]/L_b & t_{k-1} < t \le t_{k-1} + d_k t_{s,PFC} \\ i_{m1,k} = 0 & t_{k-1} + d_k t_{s,PFC} < t \le t_k \\ i_{d5,k}(t) = 0 & t_{k-1} < t \le t_{k-1} + d_k t_{s,PFC} \\ i_{d5,k}(t) = I_{k,start} + v_k T_{k,r}/L_b \\ \quad -(v_k - V_{BUS})[t - (k-1)t_{s,PFC} - d_k t_{s,PFC}]/L_b \\ t_{k-1} + d_k t_{s,PFC} < t \le t_k \\ I_{k,turnoff} = I_{k,start} + T_{k,r}/L_b & t = t_{k-1} + d_k t_{s,PFC} \\ I_{k,end} = I_{k+1,start} & t = t_k \end{cases} \tag{7}$$

$$\begin{cases} I_{L1} = \left[\dfrac{1}{2f_{line}} \displaystyle\int_0^{1/(2f_{lins})} i_{L1}^2(t) dt \right]^{0.5} \\ I_{d5} = \left[\dfrac{1}{2f_{line}} \displaystyle\int_0^{1/(2f_{lins})} i_{d5}^2(t) dt \right]^{0.5} \\ I_{m1} = \left[\dfrac{1}{2f_{line}} \displaystyle\int_0^{1/(2f_{lins})} i_{m1}^2(t) dt \right]^{0.5} \\ I_{s,PFC} = \left\{ \dfrac{1}{2f_{line}} \displaystyle\int_0^{1/(2f_{lins})} [i_{L1}(t) + i_{L2}(t)]^2 dt \right\}^{0.5} \end{cases} \tag{8}$$

2.2 Efficiency of ILPFC

Losses of EMI, rectifier, inductors, MOSFETs and diodes are denoted as P_{EMI}, $P_{b,loss}$, $P_{Lb,loss}$, $P_{m,PFC,loss}$ and $P_{d,PFC,loss}$, respectively.

2.2.1 Input EMI Filter Losses of ILPFC

As Fig. 4 shows, EMI includes capacitor C_E and inductor L_e. If $i_{AC}(t)$ is sine wave, then i_{EMI} and $P_{E,loss}$ are (9) and (10), where r_{Le} and r_{Ce} are equivalent series resistance (ESR) of C_E and L_E. I_{AC} and I_{EMI} are the RMS currents of L_E and C_E.

$$i_{EMI}(t) = i_{s,PFC}(t) - \sqrt{2}P_{o,PFC,full} \sin(2\pi f_{line}t)/V_{AC} \tag{9}$$

$$P_{E,loss} = r_{Le}I_{AC}^2 + r_{Ce}I_{EMI}^2 \tag{10}$$

2.2.2 Power Device Losses of ILPFC

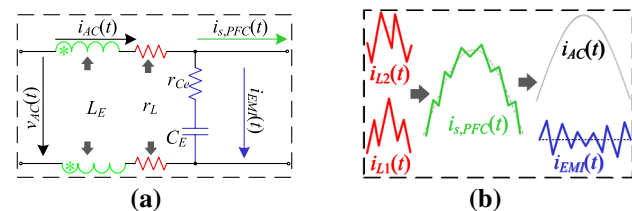The power devices` loss includes bridge loss $P_{b,loss}$, MOSFET loss $P_{m,PFC,loss}$, and diode loss $P_{d,PFC,loss}$, where $V_{b,F}$ and $V_{d,F}$ are the voltage drop of bridge and diodes. $R_{ds,on}$ is the MOSFETs` on-resistor. C_{FB} and t_{fall} are the MOSFETs` parasitic capacitance and fall time. $I_{rr}$ and $t_{rr}$ are the reverse recovering current and reverse recovery time of diodes. $P_{m,PFC,c}$ and $P_{m,PFC,s}$ are the MOSFETs` conduction loss and switching loss. $P_{d,PFC,c}$ and $P_{d,PFC,s}$ are the diodes` conduction loss and switching loss.

$$\begin{cases} P_{b,c} = V_{b,F}I_{s,PFC} \\ P_{m,PFC,c} = 2R_{ds,on}I_{m1}^2 \\ P_{d,PFC,c} = 2V_{d,F}I_{d5} \\ P_{m,PFC,s} = 2 \displaystyle\sum_{k=1}^{0.5f_s/f_{line}} \dfrac{I_{m1,turnoff}^2 t_{fall}^2}{6C_{FB}} \\ P_{d,PFC,s} = v_o I_{rr} t_{rr} f_s \\ P_{b,loss} = P_{b,c} \\ P_{m,PFC,loss} = P_{m,s} + P_{m,c} \\ P_{d,PFC,loss} = P_{d,s} + P_{d,c} \end{cases} \tag{11}$$

2.2.3 Boost Inductor Losses of ILPFC

Boost inductor`s loss is given by (12), where $S_{L_b}$, $N_{L_b}$ and $l_{L_b}$ are the effect conducting area, turn number and average winding length. $\rho_T$ is the conductor`s resistivity. The ILPFC`s efficiency can be expressed as (13), where P_{other} is mainly the driving loss. $P_{b,c}$, $P_{m,PFC,c}$ and $P_{d,PFC,c}$ are affected by I_{L1+L2}, I_{m1} and I_{d5}. $P_{m,PFC,s}$, $P_{d,PFC,s}$ are effected
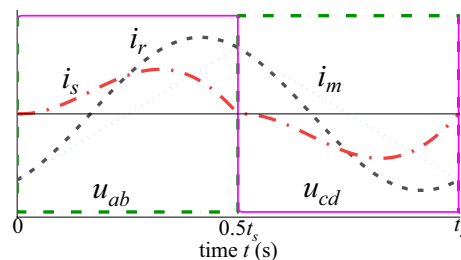

Fig. 4 EMI`s: **a** equivalent circuit, and **b** waveforms

Fig. 5 Waveforms of i_r, i_m, i_s, u_{ab}, and u_{cd} at $f_{s,LLC} = f_{r,LLC}$

by $I_{m1,k,off}$ and I_{rr}, t_{rr}. $I_{s,PFC}$, I_{m1}, I_{d5} and I_{EMI} are affected by V_{AC}, V_{BUS}, L and $f_{s,PFC}$.

$$P_{L_b,loss} = (I_{L1}^2 + I_{L2}^2)\rho_T l_{L_b} N_{L_b}/S = 2I_{L1}^2 \rho_T l_{L_b} N_{L_b}/S_{L_b} \qquad (12)$$

$$\eta_{PFC} = \frac{P_{o,PFC}}{P_{o,PFC} + P_{E,loss} + P_{L_b,loss} + P_{m,PFC,loss} + P_{d,PFC,loss} + P_{other}} \qquad (13)$$

3 LLC Resonant Converter

3.1 Waveforms of LLC Resonant Converter in P Mode

To simplify the analysis, following assumptions are taken: (a) all components are ideal devices, (b) V_o is a constant value, (c) duty cycle of $Q_3 \sim Q_6$ is 0.5. i_r, i_m, i_s, v_{ab} and v_{cd} at the resonant frequency are shown in Fig. 5. $i_r(t)$ is sinusoidal waveform. $i_m(t)$ increases in the slope of V_{BUS}/L_m during $0 \le t < 0.5t_{r,LLC}$ and decreases in the slope of $-V_{BUS}/L_m$ during $0.5t_{r,LLC} \le t < t_{r,LLC}$.

The resonant currents $i_r(t)$ and magnetizing current $i_m(t)$ are given by (14) and (15), where $I_{r,peak}$ and ω_r are the peak resonant current and angular frequency. θ is phase difference between $i_r(t)$ and v_{ab}. $\omega_r = 2\pi f_r = (L_r C_r)^{-0.5}$.

$$i_r(t) = I_{r,peak} \sin(\omega_r t - \theta) \qquad (14)$$

$$i_m(t) = \frac{V_{BUS}(4t - t_{r,LLC})}{4L_m} = \frac{V_{BUS}(4f_r t - 1)}{4f_{r1}L_m} \qquad (15)$$

Because $i_r(t) = i_m(t)$ at $t = 0$, then θ can be given by (16). The input energy $E_{V_{BUS}}$ from V_{BUS} and the absorbed energy E_R by load can be obtained by (17) and (18), where N is transformer`s turn ratio. Because $E_{V_{BUS}} = E_R$, $I_{r,peak}$ can be obtained by solving Eqs. (17) and (18), and θ can be calculated by solving Eq. (19) and (16). Moreover, because $i_s(t) = N[i_r(t) - i_m(t)]$, then teh primary and secondary RMS currents $I_{p,RMS}$ and $I_{s,RMS}$, and the turn-off current $I_{turnoff}$ can be given by (21).

$$\theta = \arcsin\left[\frac{V_{BUS}t_{s,LLC}}{4L_m I_{r,peak}}\right] = \arcsin\left[\frac{V_{BUS}}{4L_m I_{r,peak}f_r}\right] \qquad (16)$$

$$E_{V_{BUS}} = \frac{I_{r,peak}V_{BUS}}{2\pi f_r}\sqrt{\frac{V_{BUS}^2 - 16I_{r,peak}^2 L_m^2 f_r^2}{I_{r,peak}^2 L_m^2 f_r^2}} \qquad (17)$$

$$E_R = P_{o,LLC}t_{s,LLC} = \frac{V_o^2}{Rf_r} = \frac{V_{BUS}^2}{N^2 Rf_r} \qquad (18)$$

$$I_{r,peak} = \frac{V_{BUS}}{4L_m N^2 Rf_r}\sqrt{4\pi^2 L_m^2 f_r^2 + N^4 R^2} \qquad (19)$$

$$\theta = \arcsin\left[\frac{N^2 R}{\sqrt{N^4 R^2 + 4\pi^2 L_m^2 f_r^2}}\right] \qquad (20)$$

$$\begin{cases} I_{p,RMS} = \dfrac{V_{BUS}}{4\sqrt{2}L_m N^2 Rf_r}\sqrt{4\pi^2 L_m^2 f_r^2 - N^4 R^2} \\[2mm] I_{s,RMS} = \sqrt{2f_r \displaystyle\int_0^{0.5/f_r} \left[i_r(t) - i_m(t)\right]^2 N^2 dt} \\[2mm] \quad = \dfrac{V_{BUS}\sqrt{5\pi^2 N^4 R^2 - 48N^4 R^2 + 12\pi^4 L_m^2 f_r^2}}{4\sqrt{6}L_m f_r NR} \\[2mm] I_{turnoff} = \dfrac{V_{BUS}t_r}{4L_m} = \dfrac{V_{BUS}}{4f_r L_m} \end{cases} \qquad (21)$$

3.2 Losses of LLC Resonant Converter

Losses of LLC converter includes MOSFETs' loss $P_{m,LLC}$, transformer's loss P_T, resonant inductor's loss P_{Lr}, and diodes' loss. The total loss and efficiency of LLC converter are given by (26) and (27). In a half switching period, part of the reactive energy is transferred from V_{BUS} to resonant tank during $\theta/(2\pi f_r) \le t < 1/f_r$ and returns from the resonant tank to V_{BUS} during $0.5/f_r \le t < 0.5/f_r + \theta/(2\pi f_r)$ in the next half period. The reactive energy $W_{Q,Vin}$ in a switching period is given by (28), and the reactive power Q_{LLC} and power factor PF_{LLC} are given by (29) and (30). Based on FHA method, V_o can be obtained by (31) [22], where Q is the quality factor, and $k = L_m/L_r$. The selection of f_r and L_m is based on the required $P_{total,LLC}$, and C_r can be determined by (33), then L_r can be further obtained.

$$\begin{cases} P_{Q,LLC,s} = I_{turnoff}^2 t_{fall}^2 \big/ C_{FB} \\[2mm] P_{Q,LLC,c} = 2I_{p,RMS}^2 R_{ds,on} \\[2mm] P_{Q,LLC,loss} = P_{Q,LLC,s} + P_{Q,LLC,c} \end{cases} \qquad (22)$$

$$P_{T,loss} = I_{p,RMS}^2 r_{p,w} + I_{s,RMS}^2 r_{s,w} \qquad (23)$$

$$P_{L_r,loss} = I_{p,RMS}^2 r_{L_r} \qquad (24)$$
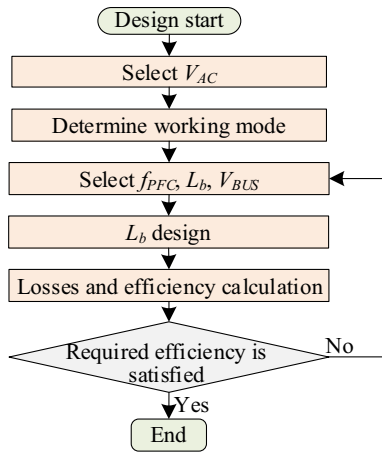
$$P_{d,LLC,loss} = 2V_F I_{s,RMS} \qquad (25)$$

Fig. 6 Design flow of ILPFC

$$P_{total,LLC,loss} = P_{L_r,loss} + P_{Q,LLC} + P_{T,loss} + P_{d,LLC}$$

$$= \frac{V_{BUS}^2 \left\{ \begin{bmatrix} 3\pi^2 R^2 N^4 r_p + (5\pi^2 - 48) N^6 R^2 r_{s,w} + 12\pi^4 (r_p + N^2 r_{s,w}) f_r^2 L_m^2 \\ +8\sqrt{6}\pi N^3 R V_F f_r L_m \sqrt{12\pi^4 L_m^2 f_r^2 + (5\pi^2 - 48) N^4 R_2} \Big/ V_{BUS} \end{bmatrix} + 6\pi^2 N^4 R^2 t_{fall}^2 L_m^2 \right\}}{96\pi^2 C_{FB} N^4 R^2 f_r^2 L_m^2} \quad (26)$$

$$\eta_{LLC} = P_{o,LLC} / (P_{o,LLC} + P_{total,LLC,loss}). \quad (27)$$

$$W_{Q,V_{in}} = \frac{V_{BUS}^2}{4\pi L_m N^2 f_r R} \left(\sqrt{4\pi^2 L_m^2 f_r^2 + N^4 R_2} - \sqrt{4\pi^2 L_m^2 f_r^2} \right) \quad (28)$$

$$Q_{LLC} = f_r W_{Q,V_{in}}$$

$$= \frac{V_{BUS}}{4 L_m f_r} \left\{ \arcsin\left(\frac{N^2 R}{\sqrt{N^4 R^2 - 4\pi^2 L_m^2 f_r^2}} \right) [2\sin^2(\pi f_r) - 1] \right.$$

$$\left. + \frac{2 L_m f_r}{N^2 R} \sin^2\left[\frac{\pi}{2} \arcsin\left(\frac{N^2 R}{\sqrt{N^4 R^2 - 4\pi^2 L_m^2 f_r^2}} \right) \right] \right\} \quad (29)$$

$$PF_{LLC} = \frac{P_{o,LLC}}{\sqrt{P_{o,LLC}^2 + Q_{LLC}^2}}$$

$$= \frac{4\pi L_m N^2 f_r R P_{o,LLC}}{\sqrt{N^4 R^2 V_{BUS}^2 - 4\pi L_m f_r V_{BUS}^4 \sqrt{4\pi^2 L_m^2 f_r^2 + N^4 R^2} + 8\pi^2 L_m^2 f_r^2 V_{BUS}^2 + 16\pi^2 L_m^2 N^4 f_r^2 R^2 P_{o,LLC}^2}} \quad (30)$$

$$V_o = \frac{V_{BUS}}{N\sqrt{\left[1 + \frac{1}{k}\left(1 - \frac{f_r^2}{f_{s,LLC}^2}\right)\right]^2 + Q^2\left(\frac{f_{s,LLC}}{f_r} - \frac{f_r}{f_{s,LLC}}\right)^2}} \quad (31)$$

$$Q = \pi^2 \sqrt{L_r/C_r} \Big/ (8N^2 R) \quad (32)$$

$$C_r = 1\Big/ 4\pi^2 f_r^2 L_r \quad (33)$$

4 Design of On-Board Charger

4.1 Design of ILPFC

The design flow of ILPFC is shown in Fig. 6. Once V_{AC}, f_{PFC}, L_b and V_{BUS} are determined, $P_{E,loss}$, $P_{b,loss}$, $P_{m,PFC,loss}$, $P_{d,PFC,loss}$ and $P_{L_b,loss}$ are calculated by the proposed method, and η_{PFC} can be improved by optimizing $f_{s,PFC}$, L_b, V_{BUS}. The design of L_b can refer to [23].

The relationships between η_{PFC} and V_{AC}, $f_{s,PFC}$, L_b and V_{BUS} are presented in the Fig. 7, where α_{PFC} is the load factor. Figure 7a shows that all loss reduces with the increase of V_{AC}. Figure 7b shows that almost all loss decreases with the increase of L_b except for $P_{Lr,loss}$, because large L_b brings large ESR and copper loss. Figure 7c shows that almost all loss decreases with the increase of $f_{s,PFC}$ except for $P_{m,PFC,loss}$ because of large switching loss. Figure 7d shows that almost all loss increases with the increase of V_{BUS} except for $P_{d,PFC,loss}$ because of large diodes` current ripple. Figure 7e shows that η_{PFC} increases with the increase of V_{AC}. Figure 7f, g present that the influence of L_b on η_{PFC} and the influence of $f_{s,PFC}$ on η_{PFC} are nonlinear. Figure 7h shows that the

influence of V_{BUS} on η_{PFC} is almost linear. High V_{BUS} can improve η_{PFC}, but which leads to high voltage stress.

4.2 Design of LLC Resonant Converter

The design flow of LLC converter is shown in Fig. 8. If V_{BUS}, $V_{o,nor}$ are determined, then N can be determined. Then the total losses can be figured out by (27), and f_r and L_m can be selected by the required $P_{total,LLC}$, and then L_r and C_r can be determined by voltage gain.

The surface map of $P_{total,LLC}$ and η_{LLC} at $f_s = f_r$ are shown in Fig. 9a, b for $R_{ds,on} = 150$ mΩ, $r_{L_r} = 25$ mΩ, $r_{p,w} = 25$ mΩ, $r_{s,w} = 22$ mΩ, $R = 31$Ω, $V_F = 0.7$ V, $t_{fall} = 6$ ns, $C_{FB} = 130$ pF. Large f_r and L_m is useful to improve η_{LLC} but reduces the voltage gain, then f_r and L_m must be optimized. If required η_{LLC} is determined, target area of (f_r, L_m) can be searched in Fig. 9b. In this paper, L_r and C_r are designed as 45 μH and 75 nF. The
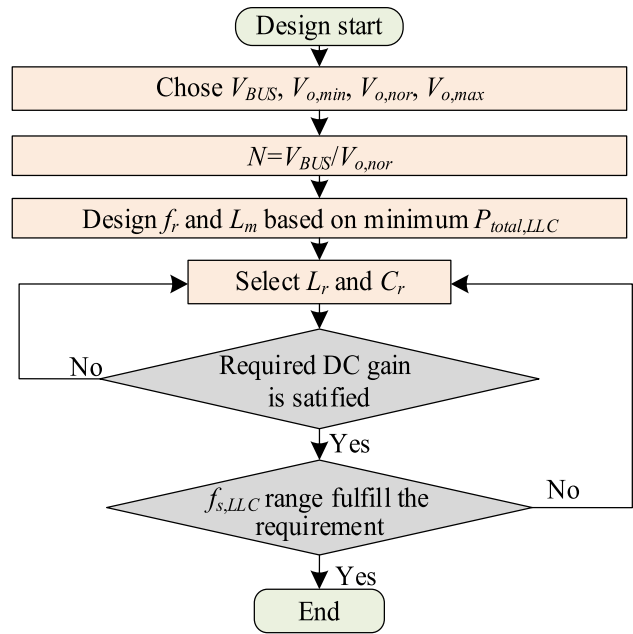

Fig. 8 Design flow chart of LLC converter

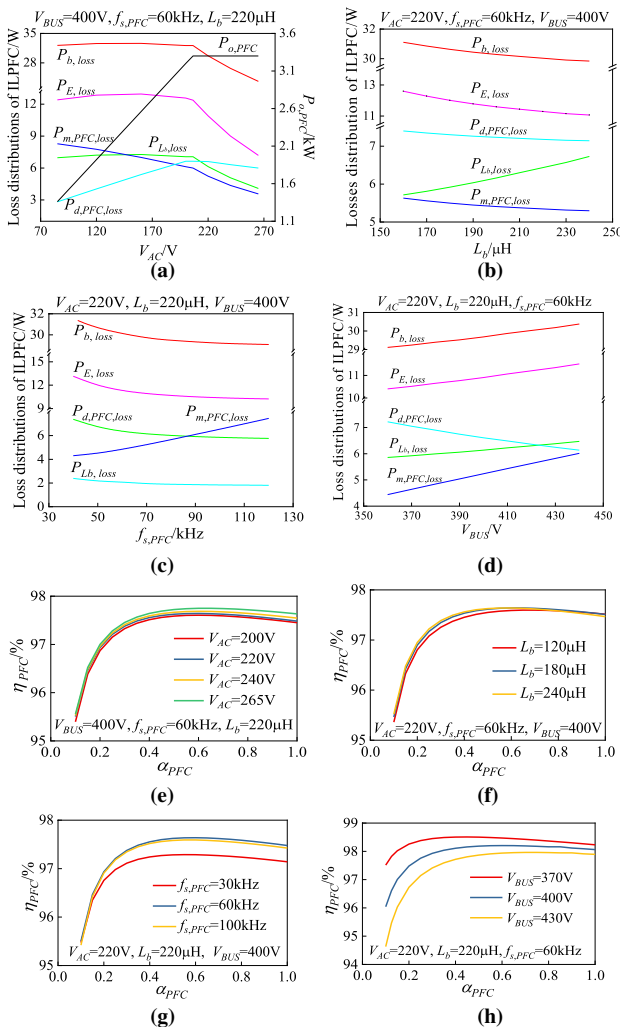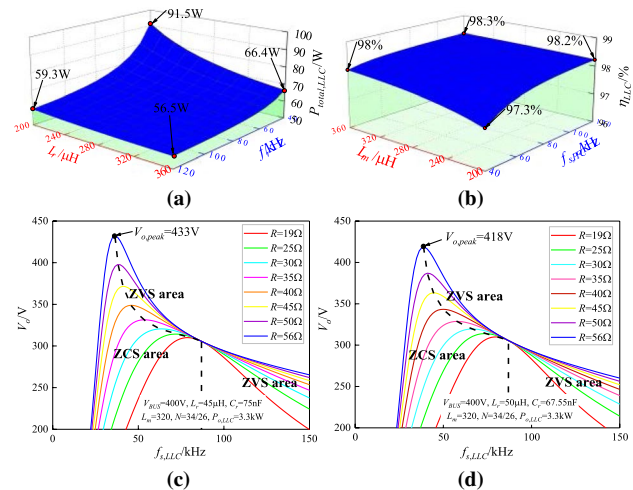**Fig. 9** Surface map of: **a** $P_{total,LLC}(f_r, L_m)$, **b** $\eta_{LLC}(f_r, L_m)$, and curves of $V_o(f_{s,LLC})$ for: **c** $L_r = 45$ μH, $C_r = 75$ nF, and **d** $L_r = 50$ μH, $C_r = 67.55$ nF

peak voltage $V_{o,peak}$ is approximate 433 V, as Fig. 9c shows, which satisfies the requirement $V_{o,max} = 430$ V. As Fig. 9d shows, if L_r and C_r are designed as 50 μH and 67.55 nF, $V_{o,peak} = 418$ V, the design result will miss the requirement.

5 Control of On-Board Charger

Average current control is used for ILPFC as shown in Fig. 10a. $V_{BUS,ref}$ is the reference of V_{bus}. $i_{L1,ref}$ and $i_{L2,ref}$ are the references of i_{L1} and i_{L2}, the duty cycles are $Temp_1$ and $Temp_2$. An offset d_{offset} is
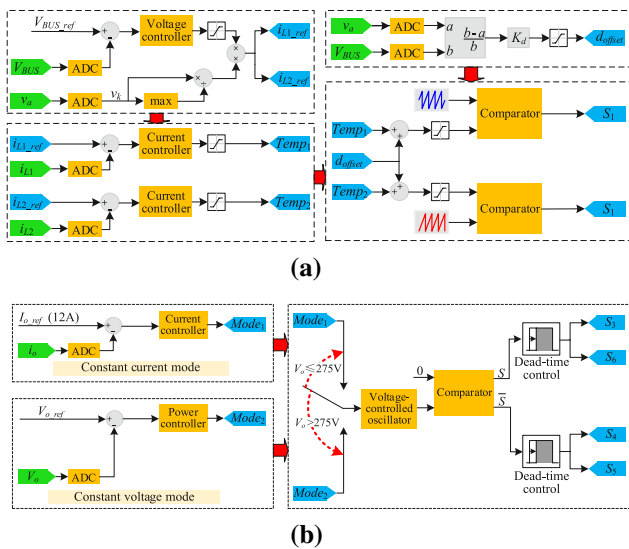

Fig. 7 Relationship between loss and: **a** V_{AC}, **b** L_b, **c** $f_{s,PFC}$, **d** V_{BUS}, and between η_{PFC} with α_{PFC} for different: **e** V_{ac}, **f** L_b, **g** $f_{s,PFC}$, and **h** V_{BUS}

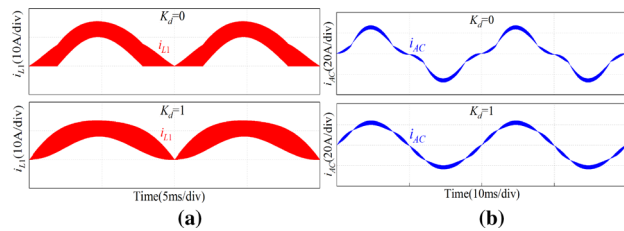**Fig. 10** Control of: **a** ILPFC, and **b** LLC converter

Fig. 11 Waveforms of: **a** i_L, and **b** i_{AC} for $K_d = 0$ and 1

added to improve PF, the modified duty cycles are $Temp_1 + d_{offset}$ and $Temp_2 + d_{offeset}$, K_d is the offset coefficient. As Fig. 11 shows, if $L_b = 220\,\mu H$ and $f_{s,PFC} = 60\,kHz$, i_{L1} is in DCM and i_{AC} is distorted near the zero crossing point for $K_d = 0$. If $K_d = 1$, i_{L1} is in CCM and i_{AC} is a sinusoidal waveform. Here K_d is set as 0.8.

$I_{o,ref}$ and $V_{o,ref}$ are the references of i_o and V_o. The charging curves is given in Fig. 12, if $V_o > 275\,V$, the charging power is 3.3 kW, the converter works in constant voltage mode, otherwise, the converter works in constant current mode, and the maximum charging current is 12A.

6 Experiment Result and Analyses

The requirements are given in Table 1. A 3.3 kW prototype is developed, as Fig. 13 shows. Two same transformers are used for LLC converter, the primary and secondary windings are in series and paralleled, the turn ratio is 17:26. PQ35/35 DMR cores are used for ILPFC, PQ35/35 DMR95 cores are used for LLC converter. TI F28035 is selected for the controller, MOSFETs with types of IPP60R099C6 and IPP65R110CFD are used for $Q_1 \sim Q_2$

and $Q_3 \sim Q_6$. In Fig. 13a, conventional OBC is based on single-phase boost PFC and LLC converter, the parameters are $L_r = 12\,\mu H$, $C_r = 99\,nF$, and $L_m = 88\,\mu H$, the size is 245 mm × 210 mm × 95 mm, the volume is 298 in^3, and the power density is 11.1 W/in^3. For this paper's prototype, the size is 241 mm × 175 mm × 75 mm, as Fig. 13b shows, the volume and power density are 193 in^3 and 7.1 W/in^3, which is higher than conventional prototype.

Measured i_{ac}, V_{ac}, i_{L1}, and i_{L2} at the full-load, half-load and 20% load states are given in Fig. 14. The normal input voltage is 220 V with 50 Hz. At the full and half load states, i_{ac} is sinusoidal and has the same phase as V_{ac}, and the PFs are higher than 99.9% and 99.8%. At 20% load state, as Fig. 14c shows, i_{L1} and i_{L2} are in DCM.

Figure 15 shows the measured waveforms of LLC converter. The maximum and minimum switching frequencies $f_{max,LLC}$ and $f_{min,LLC}$ are 117 kHz and 47.6 kHz, respectively.

Figure 16 presents the harmonic distribution at 20%, half, and full load states. The THDs at 20%, half, and full load states are 6.3%, 4.09%, and 2.98%, respectively. The PFs at 20%, half, and full load states are 96.99%, 99.91% 99.96%, respectively.

As Fig. 17a shows, measured η_{PFC} is lower than the theoretical efficiency, the error comes from the driving loss. η_{PFC}, η_{LLC} and $\eta_{overall}$ of the developed prototype are higher than conventional OBC. The PFC and LLC converters' peak efficiencies are about 97.3% and 97.4%. The overall and peak efficiencies are higher than 93.3% and 94.8% (Fig. 18).

Figure 19 shows the measured ripple factor of V_o, the ripple factor is calculated by $0.5\Delta V_o/V_o$, where ΔV_o is the peak-to-peak value of the voltage ripple, the voltage ripple factor decreases with the increase of V_o, which can be explained as follows: firstly, the voltage ripple of V_o comes from the DC-link voltage's ripple, in this paper, the peak-to-peak ripple of V_{BUS} is about 20 V, because the voltage ripple can be seen as a AC voltage, it can be transferred to V_o by the transformer, and the transformer turn ratio is about 1.308, then the peak-to-peak voltage ripple transferred from V_{BUS} to V_o is about 15.3 V. Secondly, the voltage controller of LLC converter has the ability to adjust V_o even V_{BUS} is fluctuates, then the voltage ripple transferred from V_{BUS} to V_o can be reduced, in the measured results, the peak-to-peak voltage ripple of V_o ranges from 6 to 7 V in the range of V_o from 230 to 430 V, and the voltage ripple factor is ranging from 1.39 to 0.69% as shown in Fig. 19.

Table 2 gives the hardware cost of the main components. For ILPFC, the most cost is used for inductors and capacitors, and power devices' cost also takes a great part. For LLC converter, the most part cost is used for MOSFETs and transformer. The hardware cost of ILPFC's main components is about 30.75 $, the hardware cost of LLC converter is about 40 $, the total cost of the main components is about 70.75$.

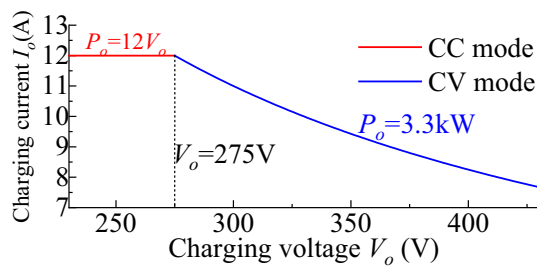The requirements are given in Table 1. A 3.3 kW prototype is developed, as Fig. 13 shows. Two same transformers

Fig. 12 Charging curve of 3.3 kW OBC

Table 1 Key parameters of 3.3 kW OBC

Parameters	Value	Parameters	Value
V_{BUS}	400 V	L_m	320 μH
P_{PFC}, $P_{o,LLC}$	3.3 kW	L_r	45 μH
$f_{s,PFC}$	60 kHz	N	1.308
f_r	86.6 kHz	V_o	230~430 V
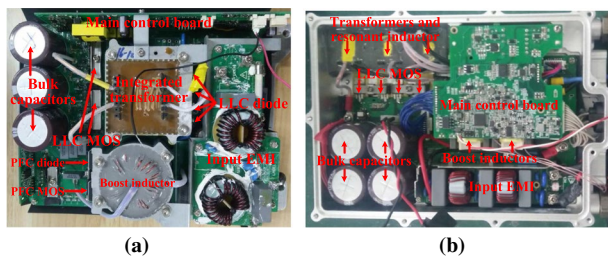
Fig. 13 Pictures of: **a** conventional, and **b** the developed 3.3 kW prototypes

Fig. 14 Measured V_{ac}, i_{ac}, i_{L1}, and i_{L2} at: **a** full, **b** half, and **c** 20% load states
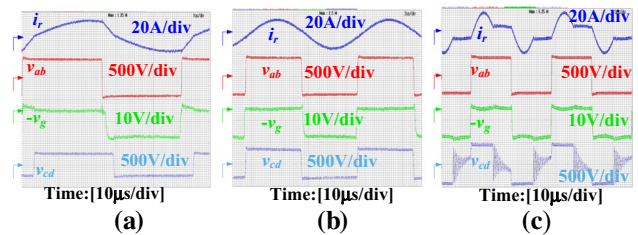
Fig. 15 Measured i_r, v_{ab}, v_{cd}, and $-v_g$ for V_o is: **a** 230 V, **b** 306 V, and **c** 430 V

are used for LLC converter, the primary and secondary windings are in series and paralleled, the turn ratio is 17:26. PQ35/35 DMR cores are used for ILPFC, PQ35/35 DMR95 cores are used for LLC converter. TI F28035 is selected for the controller, MOSFETs with types of IPP60R099C6 and IPP65R110CFD are used for $Q_1 \sim Q_2$ and $Q_3 \sim Q_6$. In Fig. 13a, conventional OBC is based on single-phase boost PFC and LLC converter, the parameters are $L_r = 12$ μH, $C_r = 99$ nF, and $L_m = 88$ μH, the size is 245 mm×210 mm×95 mm, the volume is 298 in³, and the power density is 11.1 W/in³. For this paper's prototype, the size is 241 mm×175 mm×75 mm, as Fig. 13b shows, the volume and power density are 193 in³ and 7.1 W/in³, which is higher than conventional prototype.

Table 3 shows the comparison between the developed prototypes in literatures [17, 26], where THD_{full}, PF_{full}, $\eta_{PFC,full}$, $\eta_{LLC,full}$, $\eta_{OBC,full}$ are the THD, PF, PFC's efficiency, LLC's efficiency, and overall efficiency at the full load. PD is the power density. The prototype in this paper has better performance in total efficiency, power density, THD and PF
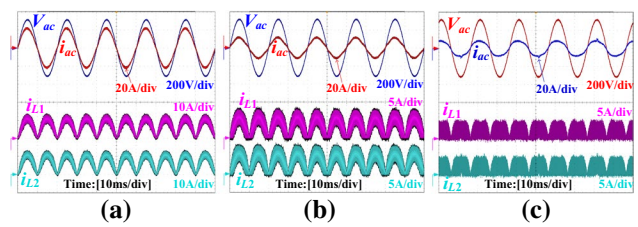
compared with the prototypes in literatures [17, 26], this is attributed to the proposed comprehensive design method to optimize OBC's internal parameters.

Table 4 shows the comparisons between this paper with literatures [1, 10, 36–38]. Compared with literatures [1, 10, 36–38], the developed prototype has higher efficiency and wider output voltage range. In literatures [1, 38], SiC-based diodes are adopted on the secondary-side, and the reverse recovery loss of SiC-based diodes is much lower than that of Si-based diodes adopted in this paper, that is to say, if the SiC-based diodes are replaced by Si-based diodes in literatures [1, 38], the advantage of efficiency in this paper over that in literatures [1, 38] will be further enhanced. Compared with this paper, the output voltage range in literature [36] is wider, however, which needs regulate dc-link voltage dynamically to ensure LLC converter always operates at the resonant frequency and sacrifices the efficiency in low output voltage region and increases the current ripple in high output voltage region. The comparison between literatures [37, 38] and the this paper is more fair, because the power is the same, but the comparison result further verified that the efficiency in this paper is higher.

7 Conclusion

The loss and efficiency of ILPFC are analyzed by the proposed discrete iterative method. The loss, efficiency and voltage gain of LLC converter are analyzed by FHA method. And the efficiency of OBC is optimized by designing the
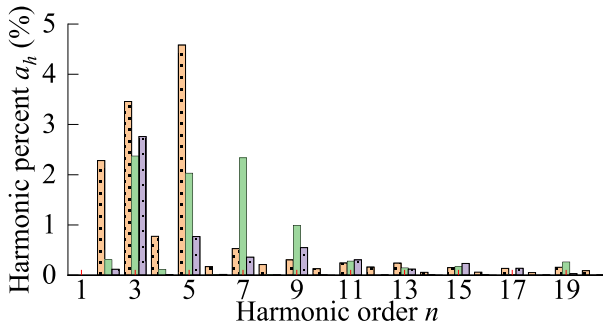
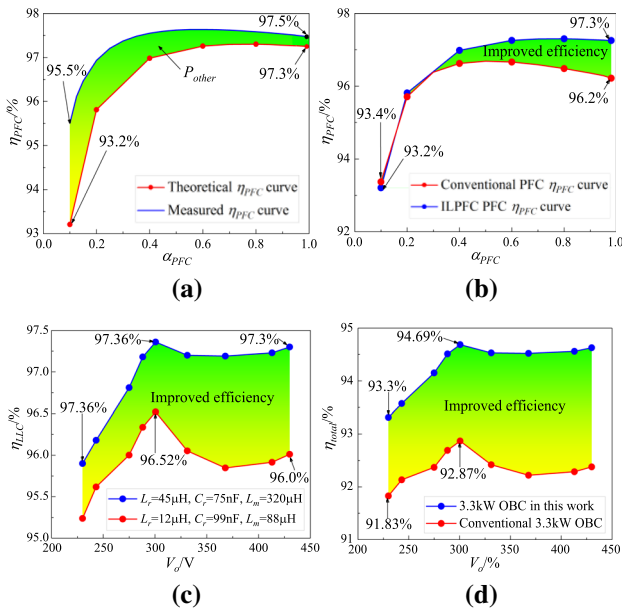**Fig. 16** Harmonic at 20%, half, and full load states

Fig. 17 Curves of: **a** η_{PFC} for theory and test, **b** η_{PFC} for two prototypes, **c** η_{LLC}, and **d** $\eta_{overall}$ for prototype
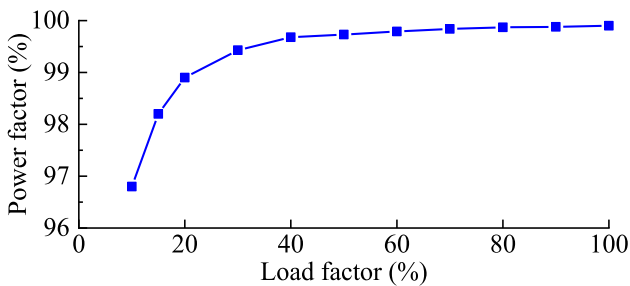

Fig. 18 Curves of relationship between power factor and load factor
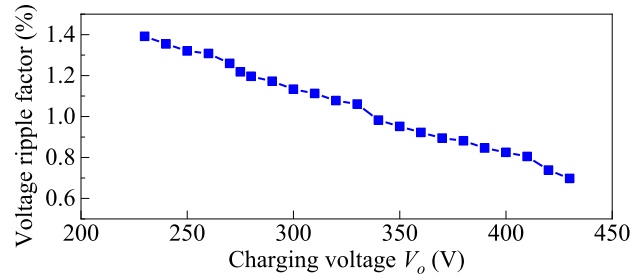

Fig. 19 Curves of relationship between voltage ripple factor and V_o

Table 2 Hardware cost of main components

Circuit	Main components` cost
ILPFC	MOSFET:5.3\$, diodes:5.7\$, driver:1.45\$, Capacitors:7.8\$, inductors:7\$, filter:3.5\$
LLC	MOSFETs:17.7\$, diodes:2.5\$, Controller:4.5\$, driver:1.7\$, filter:3\$, Resonant components:3\$, transformers:7.6\$

Table 3 Comparisons between this work and Ref. [17, 26]

Items	This paper	Ref. [17]	Ref. [26]
Topology	ILPFC+LLC	ILPFC+LLC	ILPFC+LLC
U_{ac}	220 V	220 V	110 V
U_o	203~430 V	250~450 V	320~420 V
P_o	3.3 kW	6.6 kW	1 kW
Devices	Si-based	Si-based	Si-based
THD_{full}	2.98%	Unknown	3.61%
PF_{full}	99.99%	99.4%	96.3%
$\eta_{PFC,full}$	97.3%	Unknown	96.4%
$\eta_{LLC,full}$	97.4%	95.6%	97.2%
$\eta_{OBC,full}$	94.7%	Unknown	93.7%
PD	17.1 W/in³	Unknown	131.1 W/in³

internal parameters. The ILPFC`s efficiency is improved by about 1.1% compared with conventional scheme. The efficiency of LLC converter is improved by about 1.3% compared with conventional scheme. The PF and THD of the prototype are approximate 99.99% and 2.98%, respectively, the overall efficiency is improved by about 1% compared with conventional 3.3 kW OBC at the full load state.

In the future, the proposed method will be extended to optimize the efficiency of 6.6 kW and 11 kW bi-directional OBC with properly modification for actual topologies.

Table 4 Comparisons between prototypes in this paper and references [1, 10, 36–38]

Items	This paper	Ref. [1]	Ref. [10]	Ref. [36]	Ref. [37]	Ref. [38]
Power	3.3 kW	1 kW	1 kW	1 kW	3.3 kW	3.3 kW
Dc-link voltage	400 V	390 V	390 V	100–420 V	400 V	400 V
U_o range	230–430 V	250–420 V	320–420 V	100–420 V	320–420 V	50–500 V
Peak efficiency	97.4%	96.5%	97.1%	95.9%	96.3%	96.2%
Control technology	PFM	PWM	PFM	PFM	PFM	PFM
Power devices	All Si-based	SiC diodes	Unknown	All SiC-based	SiC diodes	All Si-based

References

1. Wang H, Li Z (2018) A PWM LLC type resonant converter adapted to wide output range in PEV charging applications. IEEE Trans Power Electron 33(5):3791–3801

2. Lee I-O (2016) Hybrid PWM-resonant converter for electric vehicle on-board battery chargers. IEEE Trans Power Electron 31(5):3639–3649

3. Cheng H, Wang Z, Yang S et al (2020) An integrated SRM powertrain topology for plug-in hybrid electric vehicles with multiple driving and onboard charging capabilities. IEEE Trans Transp Electr 6(2):578–591

4. Abeywardana DBW, Hredzak PAB, Aguilera RP et al (2018) Single-phase boost inverter-based electric vehicle charger with integrated vehicle to grid reactive power compensation. IEEE Trans Power Electron 33(4):3462–3471

5. Yu F, Zhang W, Shen Y et al (2018) A nine-phase permanent magnet electric-drive-reconstructed onboard charger for electric vehicle. IEEE Trans Energy Convers 33(4):2091–2101

6. Nguyen HV, Lee D-C (2020) Integrated low-voltage charging circuit with active power decoupling function for onboard battery chargers. J Power Electron 20:1130–1138

7. Subotic I, Bodo N, Levi E (2016) Single-phase on-board integrated battery chargers for EVs based on multiphase machines. IEEE Trans Power Electron 31(9):6511–6523

8. Shi C, Tang Y, Khaligh A (2018) A three-phase integrated onboard charger for plug-in electric vehicles. IEEE Trans Power Electron 33(6):4716–4725

9. Tausif A, Jung H, Choi S (2019) Single-stage isolated electrolytic capacitor-less ev onboard charger with power decoupling. CPSS Trans Power Electron Appl 4(1):30–39

10. Wang H, Dusmez S, Khaligh A (2014) Maximum efficiency point tracking technique for LLC-based PEV chargers through variable DC link control. IEEE Trans Ind Electron 61(11):6041–6049

11. Yu F, Zhu Z, Mao J et al (2019) Performance evaluation of a permanent magnet electric-drive-reconfigured onboard charger with active power factor correction. CES Trans Electr Mach Syst 3:72–80

12. Kim D-H, Lee B-K (2017) Asymmetric control algorithm for increasing efficiency of nonisolated on-board battery chargers with a single controller. IEEE Trans Veh Technol 66(8):6693–6706

13. Nguyen HV, Lee S, Lee D-C (2019) Reduction of DC-link capacitance in single-phase non-isolated onboard battery chargers. J Power Electron 19(2):394–402

14. Liu Z, Li B, Lee FC et al (2017) High-efficiency high-density critical mode rectifier/inverter for WBG-device-based on-board charger. IEEE Trans Ind Electron 64(11):9114–9123

15. Shi C, Khaligh A (2018) A two-stage three-phase integrated charger for electric vehicles with dual cascaded control strategy. IEEE J Emerg Sel Top Power Electron 6(2):898–909

16. Khaligh A, D'Antonio M (2019) Global trends in high-power on-board chargers for electric vehicles. IEEE Trans Veh Technol 68(4):3306–3324

17. Lee J-Y, Chae H-J (2014) 6.6-kW onboard charger design using DCM PFC converter with harmonic modulation technique and two-stage DC/DC converter. IEEE Trans Ind Electron 61(3):1243–1252

18. Li H, Zhang Z, Wang S et al (2020) A 300-kHz 6.6-kW SiC bidirectional LLC onboard charger. IEEE Trans Ind Electron 67(2):1435–1445

19. Chen Y-L, Chen H-J, Chen Y-M et al (2015) A stepping on-time adjustment method for interleaved multichannel PFC converters. IEEE Trans Power Electron 30(3):1170–1176

20. Kim Y-S, Sung W-Y, Lee B-K (2014) Comparative performance analysis of high density and efficiency PFC topologies. IEEE Trans Power Electron 29(6):2666–2679

21. Marcos-Pastor A, Vidal-Idiarte E, Cid-Pastor A, Martinez-Salamero L (2016) Interleaved digital power factor correction based on the sliding-mode approach. IEEE Trans Power Electron 31(6):4641–4653

22. Ta LAD, Dao ND, Lee D-C (2020) High-efficiency hybrid LLC resonant converter for on-board chargers of plug-in electric vehicles. IEEE Trans Power Electron 35(8):8324–8334

23. Kucka J, Dujic D (2021) Equal loss distribution in duty-cycle controlled H-bridge LLC resonant converters. IEEE Trans Power Electron 36(5):4937–4941

24. Liu F, Ruan X, Huang X, Qiu Y (2021) Second harmonic current reduction for two-stage inverter with DCX-LLC resonant converter in front-end DC–DC converter: modeling and control. IEEE Trans Power Electron 36(4):4597–4609

25. Li Z, Xue B, Wang H (2020) An interleaved secondary-side modulated LLC resonant converter for wide output range applications. IEEE Trans Ind Electron 67(2):1124–1135

26. Wang H, Dusmez S, Khaligh A (2014) Design and analysis of a full-bridge LLC-based PEV charger optimized for wide battery voltage range. IEEE Trans Veh Technol 63(4):1603–1613

27. Ishikawa K, Mochizuki Y, Higuchi K, Jirasereeamornkul K, Chamnongthai K (2014) Design of approximate 2-degree-of-freedom controller for interleaved PFC boost converter. In: 2014 proceedings of the SICE annual conference (SICE)

28. Nguyen HV, Lee D-C, Blaabjerg F (2021) A novel SiC-based multifunctional onboard battery charger for plug-in electric vehicles. IEEE Trans Power Electron 36(5):5635–5564

29. Zhu L, Bai H, Brown A et al (2020) Transient analysis when applying GaN + Si hybrid switching modules to a zero-voltage-switching EV onboard charger. IEEE Trans Transp Electr 6(1):146–157

30. Li S, Lu S, Mi CC (2021) Revolution of electric vehicle charging technologies accelerated by wide bandgap devices. Proc IEEE 190(6):985–1003

31. Seo G-S, Le H-P (2020) S-Hybrid step-down dc–dc converter—analysis of operation and design considerations. IEEE Trans Ind Electron 67(1):265–275

32. Reddy PVV, Suryawanshi HM, Talapur GG et al (2019) Optimized resonant converter by implementing shunt branch element

as magnetizing inductance of transformer in electric vehicle chargers. IEEE Trans Ind Appl 55(6):7471–7480

33. Nguyen HV, To D-D, Lee D-C (2018) Onboard battery chargers for plug-in electric vehicles with dual functional circuit for low-voltage battery charging and active power decoupling. IEEE Access 6:70212–70222

34. Mallik A, Lu J, Khaligh A (2018) Sliding mode control of single-phase interleaved totem-pole PFC for electric vehicle onboard chargers. IEEE Trans Veh Technol 67(9):8100–8109

35. Wang C, Chu S, Yu H et al (2022) Control strategy of unintentional islanding transition with high adaptability for three/single-phase hybrid multimicrogrids. Int J Electr Power Energy Syst 136(107724):1–12

36. Shi C, Wang H, Dusmez S, Khaligh A (2017) A SiC-based high-efficiency isolated onboard PEV charger with ultrawide DC-link voltage range. IEEE Trans Ind Appl 53(1):501–511

37. Sun W, Jin X, Zhang L et al (2017) Analysis and design of a multi-resonant converter with a wide output voltage range for EV charger applications. J Power Electron 17(4):849–859

38. Shen Y, Zhao W, Chen Z et al (2018) Full-bridge LLC resonant converter with series-parallel connected transformers for electric vehicle on-board charger. IEEE Access 6:13490–13500

Publisher's Note Springer Nature remains neutral with regard to jurisdictional claims in published maps and institutional affiliations.

Fei Xue was born in Guyuan City, China, in 1994. He received B.E and M.S degree in electrical engineering from Tianjin University, China, in 2014 and 2016. He currently is an engineer in Electric Power Research Institute, State Grid Ningxia Electric Power Company (NEPC), Ningxia, China. He is the author/coauthor of 3 books and more than 50 publications in technical journals and conferences. His research interest includes renewable energy, and modeling and planning of distribution network.

Xin Ma was born in Wuzhong City, China, in 1994. He received B.E and M.S degree in electrical engineering from Zhejiang University, China, in 2016 and 2019. He currently is an engineer in Electric Power Research Institute, State Grid Ningxia Electric Power Company (NEPC), Ningxia, China. He is the author of more than 15 publications in technical journals and conferences. His research interest includes renewable energy, and planning and dispatching of distribution network.

safety and stability analysis

simulation.

Hongqiang Li was born in Zhongwei City, China, in 1990. He received B.E and M.S degree in electrical engineering from Southwest Jiaotong University, China, in 2011 and 2014. He currently is a senior engineer in Electric Power Research Institute, State Grid Ningxia Electric Power Company (NEPC), Ningxia, China. He is the author/coauthor of 3 books and more than 10 publications in technical journals and conferences. His research interest includes renewable energy, and power system

Di Zhang was born in Yinchuan City, China, in 1991. He received B.E and M.S degree in electrical engineering from University of Electronic Science and Technology of China, in 2013 and 2016. He currently is an engineer in Electric Power Research Institute, State Grid Ningxia Electric Power Company (NEPC), Ningxia, China. He is the author/coauthor of 3 books and more than 10 publications in technical journals and conferences. His research interest includes renewable energy, and power system

Hengshan Xu was born in Ankang City, China, in 1989. He received B.E and Ph.D. degrees from Northwest Agricultural & Forestry University (NWAFU) and North China Electric Power University (NCEPU), in 2012 and 2018. He currently is with College of Electrical Engineering & New Energy, China Three Gorges University (CTGU), China. His research interest includes active power factor correction, resonant converter, new energy generation, etc.

Lei Zhou was born in Guyuan City, China, in 1992. He received B.E and M.S degree in electrical engineering from Tianjin University, China, in 2015 and 2018. He currently is an engineer in Electric Power Research Institute, State Grid Ningxia Electric Power Company (NEPC), Ningxia, China. His research interest includes renewable energy, and modeling and planning of distribution network.

Chao Wang was born in Yin-Chuan City, China, in 1989. He received B.E and Ph.D. degree from Xi'an Jiaotong University, China, in 2011 and 2017. He currently is an engineer in Electric Power Research Institute, State Grid Ningxia Electric Power Company (NEPC), Ningxia, China. His research interest includes renewable energy, and modeling and planning of distribution network.